



LETTER • OPEN ACCESS

Pinning forces of sliding drops at defects

To cite this article: Alexander Saal *et al* 2022 *EPL* **139** 47001

View the [article online](#) for updates and enhancements.

You may also like

- [The drying of liquid droplets](#)
Zechao Jiang, , Xiuyuan Yang et al.
- [Frequency-dependent transient response of an oscillating electrically actuated droplet](#)
S Dash, N Kumari and S V Garimella
- [A phenomenological approach to the deposition pattern of evaporating droplets with contact line pinning](#)
Haiqin Wang, Dadong Yan and Tiezheng Qian

Pinning forces of sliding drops at defects

ALEXANDER SAAL, BENEDIKT B. STRAUB, HANS-JÜRGEN BUTT and RÜDIGER BERGER^(a) 
Max Planck Institute for Polymer Research - Ackermannweg 10, 55128 Mainz, Germany

received 22 April 2022; accepted in final form 21 June 2022

published online 22 August 2022

Abstract – Wetting of surfaces depends critically on defects which alter the shape of the drop. However, no experimental verification of forces owing to the three phase contact line deformation at single defects is available. We imaged the contact line of sliding drops on hydrophobic surfaces by video microscopy. From the deformation of the contact line, we calculate the force acting on a sliding drop using an equation going back to Joanny and de Gennes (*J. Chem. Phys.*, **81** (1984) 554). The calculated forces quantitatively agree with directly measured forces acting between model defects and water drops. In addition, both forces quantitatively match with the force calculated by contact angle differences between the defect and the surface. The quantitative agreement even holds for defects reaching a size of 40% of the drop diameter. Our validation for drop's pinning forces at single defects is an important step towards a general understanding of contact line motion on heterogeneous surfaces.



Copyright © 2022 The author(s)

Published by the EPLA under the terms of the [Creative Commons Attribution 4.0 International License](https://creativecommons.org/licenses/by/4.0/) (CC BY). Further distribution of this work must maintain attribution to the author(s) and the published article's title, journal citation, and DOI.

Introduction. – A drop sliding over a surface forms an advancing contact angle at the front Θ_a^s and a receding contact angle at the rear Θ_r^s . The difference of both contact angles is called contact angle hysteresis (CAH) [1–3]. CAH is the reason why drops can rest on inclined surfaces although gravity is acting on the drops. In addition, CAH is associated with topographical and chemical heterogeneities of surfaces [4,5]. Inhomogeneities ranging from the nanometer up to μm -scale play a major role [4]. They lead to pinning of the three-phase contact line, hereinafter referred to as contact line. Pinning of the contact line increases the CAH and therefore opposes forces leading to sliding of the liquid. Although models describing pinning forces of liquids from a surface defect have existed for 40 years, no experimental validation of forces is available. Therefore, we adapt a theory originated from Joanny and de Gennes [6] and calculate and measure the force acting between model defects and water drops.

Pinning of contact lines of surfaces containing a model defect are typically studied by Wilhelmy plate experiments. A flat substrate is drawn into or out of a bath of liquid (fig. 1(a)) [4,6–9]. The interaction of the model defect results in a contact line deformation (CLD) close to the defect and changes the local potential arising from the

surface tension of the liquid. The latter causes a restoring force due to fringe elasticity. Thus, the more the contact line is pulled away from the equilibrium position in the y -direction, the higher the force F_{CLD} that acts on the defect will be. Therefore, measurements of the shape of the contact line $\eta(x)$, for example by optical microscopy, allow calculating the force acting on the defect [7].

Joanny and de Gennes derived a relation between the shape of the contact line $\eta(x)$ and the corresponding force F_{CLD} for an infinitely small defect on a hydrophilic surface withdrawn from a liquid bath [6],

$$\eta(x) = \frac{F_{\text{CLD}}}{\pi\gamma\Theta_0^2} \ln\left(\frac{L}{x}\right) = \frac{F_{\text{CLD}}}{k}. \quad (1)$$

Here γ is the surface tension, Θ_0 is the equilibrium contact angle of the liquid with the flat surface and L is a large-scale cut-off length. The term $k = \pi\gamma\Theta_0^2/\ln(L/x)$ with a unit N/m. Nadkarni and Garoff associated L to the capillary length of the liquid $\lambda_c = \sqrt{\gamma/\rho g}$ (ρ is the density of the liquid and g is the gravitational acceleration), which is about 2.73 mm for water in air at ambient temperature [7]. Later on, alternative theoretical derivations confirmed eq. (1) [10].

Several groups studied CLD at defects on otherwise flat substrates upon removing the substrate from a liquid bath [7,11]. Based on the measurements of CLD,

^(a)E-mail: berger@mpip-mainz.mpg.de (corresponding author)

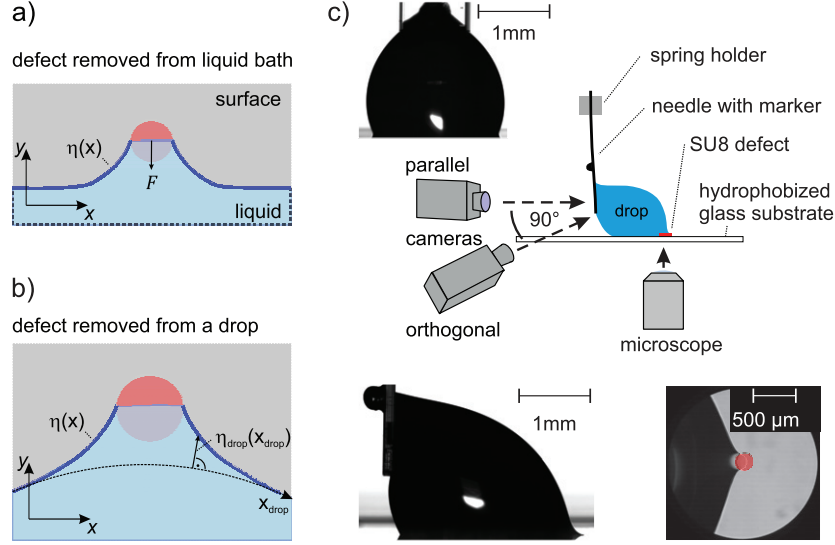


Fig. 1: (a) Schematic drawing of a round defect on a surface that is removed from a liquid bath. (b) Schematic image of the rear side of a drop being pulled over a round defect in top view. The drop slides in the $-y$ -direction and the contact line deforms by $\eta(x)$. Relative to the undisturbed drop's contact line it deforms by $\eta_{\text{drop}}(x_{\text{drop}})$. The position $x = 0$ corresponds to the center of the defect. (c) Schematic drawing of the used setups: A drop slides across a hydrophobized glass surface with a hydrophilic SU8 model defect. Two cameras are mounted orthogonal and parallel to the sliding direction to record the deflection of a glass needle and the drop shape. A transmission light microscope records the receding three-phase contact line. For technical reasons the parallel/orthogonal view experiments are performed subsequently in two different setups. The contact line measurements are performed by moving the spring holder from right to left, resulting in a stationary sample position. The direct force measurements are performed by moving the sample from left to right, resulting in a stationary spring holder.

eq. (1) was used to calculate the forces acting on a single defect. Nadkarni and Garoff studied different sizes of heterogeneities on hydrophobic substrates, which revealed that the elastic response follows Hooke's law [7]. Marsh and Cazabat imaged CLD when a plate with defects made by pen ink was removed vertically from a silicon-oil bath [11]. These studies show that the CLD can be fitted by eq. (1) but also deviations occur due to uncertainty of the contact angles along the contact line.

All experimental studies based on Joanny's and de Gennes' theory lack verification and quantification of the calculated force arising from CLD. Pinning forces of nanometric defects were investigated by atomic force spectroscopy, however lacking measurements of the CLD [12]. Pinning forces while removing a drop vertically from the surface have been detected on superhydrophobic surfaces [13]. Furthermore, forces for laterally sliding drops were investigated with a setup that is based on measuring the deflection of a bendable capillary [14,15]. Pilat *et al.* and Qiao *et al.* used such a setup to study lateral adhesion forces of micropillar arrays [14,15]. Here, Qiao *et al.* qualitatively depicted occurring multiple CLD while the drop is sliding over the micropillar array [15]. Mugele *et al.* used a capillary force sensor to measure the pinning strength of electrowetting traps [16]. However, the forces exerted by contact line deformation on defects and drops have never been quantitatively compared and analyzed for sliding drops. In order to validate the model of Joanny and de Gennes, we first analyze the shapes of the three

phase contact lines optically at the receding side of a drop and calculate the pinning force of strong defects using a refined model that goes back to the model of Joanny and de Gennes. In addition we carry out lateral drop adhesion force measurements (DAFI) [14], allowing us to measure pinning forces of defects directly. Finally, we show that forces resulting from an analytical model which is based on contact angle hysteresis match the forces calculated from CLD and from DAFI. Forces arising from CAH are given by the capillary equation [17–20], where the drop's sliding force F_c corresponds to

$$F_c = \kappa w \gamma (\cos \Theta_r^s - \cos \Theta_a^s). \quad (2)$$

Here, w is the width of the contact area of the drop. Typically a κ -factor ($\kappa \leq 1$) is added to the equation, which accounts for the shape of the drop [21–23].

Notably, despite different theoretical approaches all three evaluations result in the same force for identical defects. Moreover, extrapolating the force to an infinitesimal small defect resulted in a quantitative validation of Joanny's and de Gennes' model.

Sample preparation. – Cylindrical model defects (radius: 50–500 μm , height: 10 μm) were prepared in SU8-layers by photolithography on glass cover slips. Then we exposed the surface to the vapor of perfluorooctyl-silane (trichloro(1H,1H,2H,2H-perfluorooctyl)silane (PFOTS)). Such sample surfaces have advancing contact angles of $117 \pm 2^\circ$ and receding angles of $90 \pm 5^\circ$ (the Supplementary

Material Supplementarymaterial.pdf (SM), section “S1 sample preparation”). The shape of the contact line of the sliding drop is measured by an inverted transmission light microscope in combination with a high speed camera which is mounted underneath the transparent substrate (fig. 1(c)). In this setup, the glass needle drags the drop, while the sample stays fixed at the same place (see the SM, section “S2 inverse optical microscope setup”). This arrangement has the advantage that defects can be positioned in the center of the image (fig. 1(c), bottom right image).

Force by Contact Line Deformation. – To investigate the time-dependent CLD, *i.e.*, $\eta(x, t)$ of a water drop sliding across model defects, we first discuss the experiment of a defect having a radius of $100\,\mu\text{m}$ (fig. 2(a)). The edge of the defect relative to the apex of the undeformed receding contact line corresponds to $s = v_{\text{drop}} \cdot (t_{\text{frame}} - t_0)$. Here, we set t_0 to an offset value so that $t_{\text{frame}} - t_0 = t$ becomes zero when the defect’s apex side reaches the contact line. The first snapshot of the movie taken at $s = -271\,\mu\text{m}$ corresponds to the defect that is fully immersed in the drop and is still far away from the contact line (fig. 2(a), stage *I*). At this stage, the contact line is undistorted by the model defect. As long as the defect is $< -20\,\mu\text{m}$ away from the contact line, all contact lines look similar in shape and they can be fitted by elliptical arcs. For all these contact lines both radii of the ellipse are identical while the center position changes with the sliding speed of the drop. Once the defect is closer than $-20\,\mu\text{m}$ from the contact line, we observed a jump of the contact line to the model defect (fig. 2(a), stage *II*). Hereafter, the three phase contact line deforms more and more (fig. 2(a), stages *III* to *V*) until it detaches from the model defect at $s > 360\,\mu\text{m}$ ($= 2.6\,\text{s}$) (after stage *V*). After the detachment the contact line has an identical curvature compared to $s = -271\,\mu\text{m}$.

From the series of images recorded with the high speed camera, we calculate the difference of the contact line to the unperturbed, curved contact line. Firstly, the position of the undeformed contact line of the drop is shifted linearly to the corresponding time of the frame of the deformed contact line. Secondly, for every point of the deformed contact line the distance (length of the normal vector sitting on the ellipse) to the contact line of the drop is calculated (fig. 1(b)). This calculation results in the experimental deformations $\eta_{\text{drop}}(x_{\text{drop}})$ for every point along the undeformed, curved contact line (x_{drop}), exemplarily plotted for the different situations *II*–*V* (fig. 2(b)).

Equation (1) was derived by considering an infinitely small defect on a hydrophilic surface, which is moved out of an extended water bath [6]. In analogy, for hydrophobic surfaces with a receding contact angle of 90° ($\sin \Theta_r^s = 1$) de Gennes, Brochard-Wyart and Quéré [24] deduced

$$\eta(x) = \frac{F_{\text{CLD}}}{\pi\gamma} \ln\left(\frac{L}{x}\right). \quad (3)$$

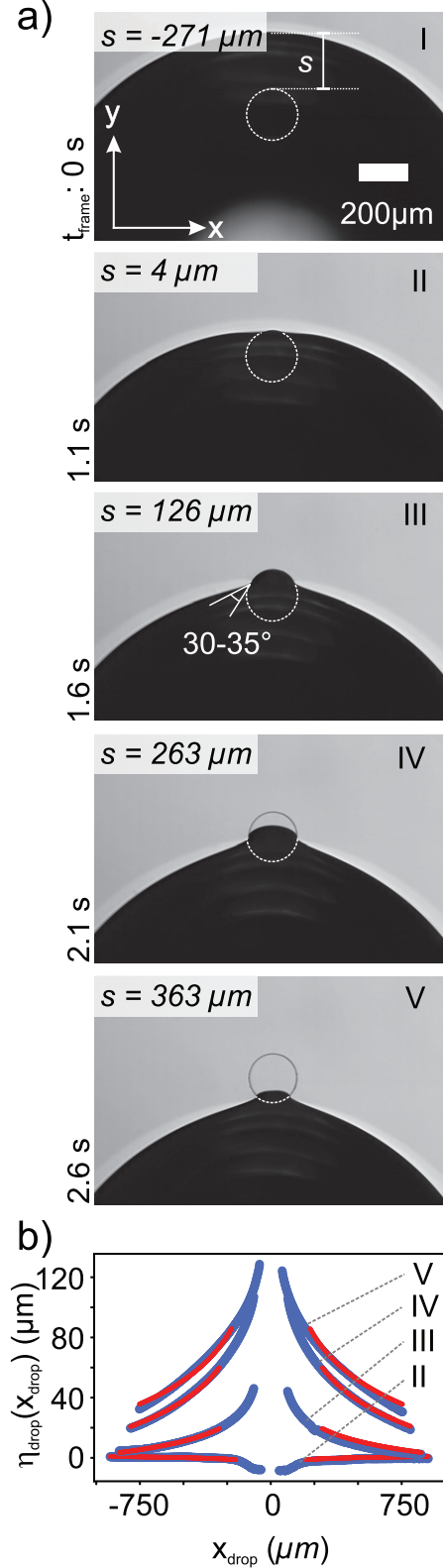


Fig. 2: (a) Transmission light microscope images of the drop sliding across a cylindrical model defect having a radius of $100\,\mu\text{m}$. This defect is situated in the center of the optical image. The drop has a volume of $5\,\mu\text{L}$. (b) The experimentally determined projected $\eta_{\text{drop}}(x_{\text{drop}}, t)$ and the fit $\eta_{\text{drop,fit}}(x_{\text{drop}}, t)$ based on eq. (4) are shown in blue and red color, respectively.

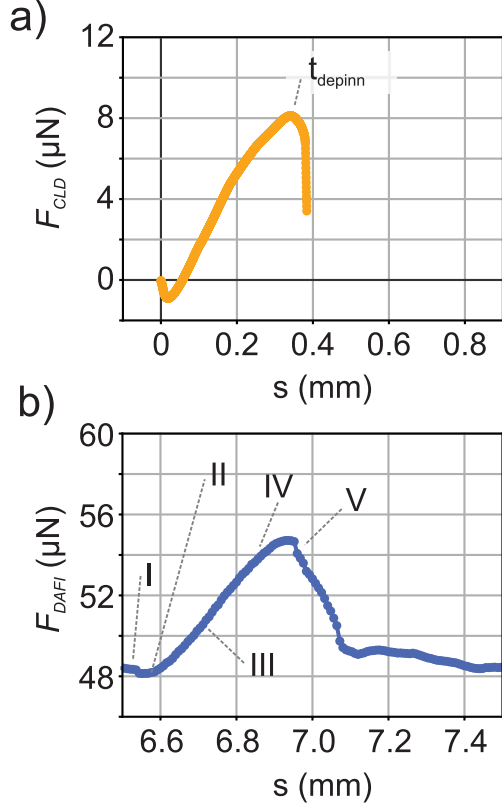


Fig. 3: Comparison of the force *vs.* position (a) measured by the CLD $\eta_{\text{drop,fit}}(x_{\text{drop}})$ and (b) measured by DAFI. Volumes of $5 \mu\text{L}$ were used for both measurements. Both measurements were performed subsequently in two setups (fig. 1). The dynamics after depinning is given by the relaxation of the local contact line (approximately 20 ms) (a). The dynamics after depinning in the DAFI measurements (b) includes relaxation of the additional elongation of the drop due to pinning. After depinning from the defect, the relaxation of the entire contact line into a steady state is much slower (approximately 1 second).

In our notation, a CLD in the $+y$ -direction ($\eta(x) > 0$) causes a force $F_{\text{CLD}} > 0$ acting on the drop, *i.e.*, in the $+y$ -direction (the force acting on the defect is in the $-y$ -direction). Thus, $L/x > 1$. We refine eq. (3) by adding the parameter $x_d(t)$ to fit the measured contact line of the drop. This parameter represents the measured defect width at the position of the contact line. In order to account for small elongations of the entire drop owing to interactions with the defect, we include the parameter $\eta_{\text{off}}(t)$. In the refined equation

$$\eta_{\text{drop,fit}}(x_{\text{drop}}, t) = \eta_{\text{off}}(t) + \frac{F_{\text{CLD}}(t)}{\pi\gamma} \ln\left(\frac{\lambda_c}{|x_{\text{drop}}| - x_d(t)/2}\right), \quad (4)$$

we use the capillary length λ_c of water and the absolute value of x_{drop} to fit CLDs at both sides from the defect center. We also extracted the defect width $x_d(t)$ from the recorded video. Equation (4) was fitted to

all $\eta_{\text{drop}}(x_{\text{drop}}, t)$ extracted from the video and the force resulting from the fitted F_{CLD} was plotted *vs.* defect position s (fig. 3(a)). When the defect touches the contact line, F_{CLD} increases until the three phase contact line slips over the defect at $s = 300\text{--}360 \mu\text{m}$ and finally detaches at $s = 390 \mu\text{m}$. We observed a deviation from the linear regime towards lower forces for an extensions $> 200 \mu\text{m}$. Such non-linear deviations have been predicted by computations [25]. In addition, we attribute the decrease in F_{CLD} at higher forces to contact line sliding along the cylindrical defect reducing η_{drop} . The maximum force is reached at $F_{\text{max}} = 8 \mu\text{N}$. Normalizing this value $F_{\text{max}}/\pi\gamma$ results in $35 \mu\text{m}$. This value is of the same order as the normalized maximum pinning force of polymethylmethacrylate beads with a diameter of $200 \mu\text{m}$ placed on a polystyrene film ($40\text{--}50 \mu\text{m}$) [7] (see the SM, section “S3 dimensionless force values compared to literature”). After the maximum force is reached, the defect width at the contact line x_d decreases, which indicates sliding of the contact line across the defect until it detaches (see the SM, section “S4 defect width x_d as seen by contact line after projection”). Thereafter, the contact line returns to the initial shape within 0.25 s. A central question in this work is, if F_{CLD} , calculated by eq. (4), will correspond quantitatively to the force that acts on a drop while it slides over the surface with this defect. Therefore, we performed direct force measurements using DAFI.

Direct force measurement. – The DAFI [14,16,26] consists of a rectangular glass needle (length 5 cm, width 1 mm), which holds the drop and deflects while the drop is sliding over a surface. A linear stage moves the substrate relative to the drop. Two cameras (Baumer VCXU-50M, a maximum resolution of 5 MP) record drop shape in front and side view and needle deflection in a shadowgraphy configuration (fig. 1(c)). The deflection of the glass needle u_n is extracted from the video recorded in side-view. We use Hooke’s law to calculate the force acting on the spring by $F_{\text{DAFI}} = k_n \cdot u_n$ where k_n is typically around $0.2 \pm 0.02 \text{ N/m}$ (see the SM, section “S5 DAFI: Spring calibration” and section “S6 force extraction”). In particular, F_{DAFI} measurements do not require information on CLD nor contact angles of involved surfaces.

The direct force measurement of a sliding drop over a defect having a width of $200 \mu\text{m}$ and a height of $10 \mu\text{m}$ — same as above — showed a constant lateral force $F_{\text{DAFI}}(t)$ of $48\text{--}49 \mu\text{N}$ as long as the contact line remains undeformed (fig. 3(b)). The latter is the case for the defect inside the drop and away from the three phase contact line. Our surface exhibits an advancing contact angle Θ_a^s and a receding angle Θ_r^s of $117 \pm 2^\circ$ and $90 \pm 5^\circ$, respectively, and the width of the drop is 2 mm (see the SM, section “S7 contact angle extraction”). Accordingly, we calculated a sliding force F_c of $49 \pm 17 \mu\text{N}$ ($\kappa = 1$) using eq. (2), which is in good agreement with our experimental values.

At the position where the cylindrical defect comes close to the contact line from the liquid phase, the contact

line jumps onto the defect (marked with II in fig. 2(a) and fig. 3(b)). At this stage, we measured a negative force $F_{\text{DAFI},II}$ of $-0.25 \mu\text{N}$, indicating that the contact line is pulled towards the defect. Then the force increases linearly. After reaching a maximum force of $55 \mu\text{N}$ the drop detaches from the defect. Subtracting the sliding force of $48 \mu\text{N}$ results in $7 \mu\text{N}$ maximum force due to pinning of the contact line at the defect. We repeated the DAFI measurement three to five times with different drops of the same volume and determined an average maximum pinning force of the three phase contact line of $F_{\text{DAFI}} = 7.3 \pm 1.9 \mu\text{N}$. This value is in agreement with the average force calculated by the contact line deformation. After the maximum force is reached, the measured force decays to a value of $48\text{--}49 \mu\text{N}$. In conclusion, the measured forces by DAFI agrees with the calculated forces based on the measured CLD (eq. (4)). The optical method for measuring local CLD reflects the force that acts on the defect at a given time. DAFI measurements reflect all forces acting on the drop and include global changes in CL. The latter is visible in the longer force tail after depinning from the defect. Thus a one-to-one correlation of forces extracted from local CLD and drop force measurements is not given at abruptly appearing instabilities.

Capillary force model. – Both DAFI and CLD measurements can be applied to study pinning forces of defects with arbitrary shapes. In the case of cylindrically shaped defects, as in our case, we can calculate the force based on geometrical considerations and capillary forces exerted by the defect (eq. (2)). For cylindrical defects, the pinning force is composed of two contributions: The first one is the pinning force at both side walls $F_{\text{wall}}^{\text{d}}$ with height H and receding contact angle Θ_r^{d} ,

$$F_{\text{wall}}^{\text{d}} = 2H\gamma \sin(\alpha - \Theta_r^{\text{d}}), \quad (5)$$

where α is the angle between the front side of the cylindrical defect and the contact line pinned to the defect (fig. 4(a)). The second contribution comes from receding contact angle differences of the defect Θ_r^{d} and the substrate Θ_r^{s} on top of the circular shape

$$F_{\text{top}}^{\text{d}} = w_a \gamma (\cos \Theta_r^{\text{d}} - \cos \Theta_r^{\text{s}}), \quad (6)$$

where $w_a = 2R \sin \alpha$ is the width of the contact line on the top face of the defect (fig. 4(a)) (see the SM, section “S8 geometrical approximation, error calculation”). In our case we have a water drop on a surface with $\Theta_r^{\text{s}} = 90 \pm 5^\circ$. The receding contact angles on the cylinder surfaces of the defect Θ_r^{d} are measured by taking side view optical images (see the SM section “S7 contact angle extraction”). In the case of our cylindrical model, the defect’s radius R is one order of magnitude larger than its height H . Therefore, $F_{\text{top}}^{\text{d}}$ dominates the force. The maximum force is obtained when the contact line stretches over the full width of the defect, *i.e.*, $\alpha = 90^\circ$ (see the SM, section “S9 the force reaches theoretical maximum at $\alpha = 90^\circ$ ”).

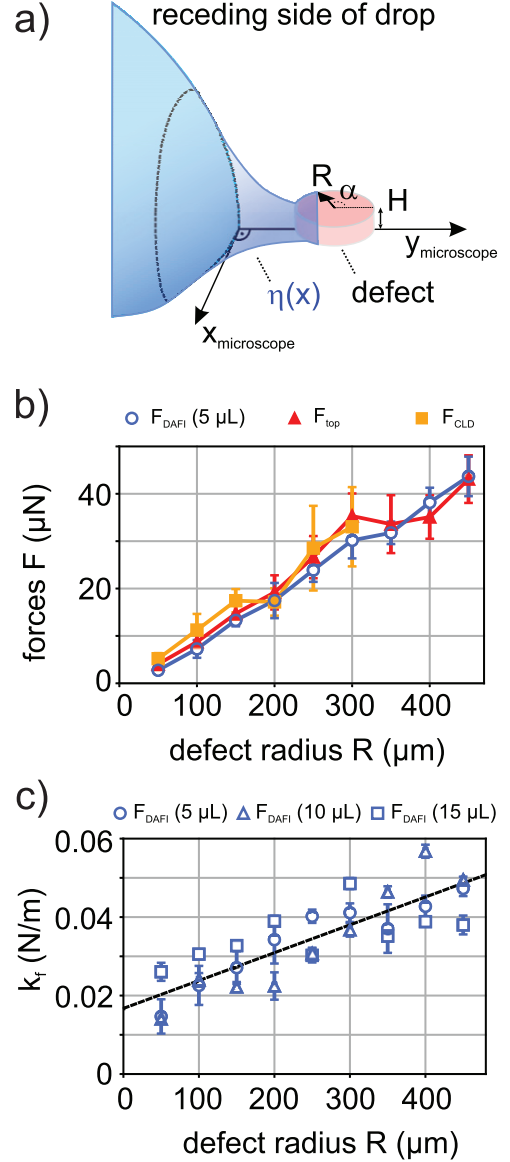


Fig. 4: (a) Schematic side-view of the deformation of a contact line $\eta(x, t)$ at a hydrophilic cylindrical defect on a hydrophobic surface interacting at the receding side of a drop. The cylindrical defect (red color) has a height, H and a radius R . The position of the receding contact line on the top face of the defect is described by an angle α . (b) Summary of depinning forces measured by CLD, DAFI and our geometrical consideration. (c) Spring constant of the fringe of the drop’s contact line measured by DAFI. The increase in force during the pinning process was fitted for each measurement and then averaged over the dataset. Errors correspond to the standard deviation within one dataset (minimum three independent measurements). The red line is a linear fit to all data points. The fitted line has a y -intercept of $0.017 \pm 0.33 \text{ N/m}$.

Thus, the maximum force becomes directly proportional to the defect width. For a defect with a radius $R = 100 \mu\text{m}$ and a $\Theta_r^{\text{s}} = 90 \pm 5^\circ$ and $\Theta_r^{\text{d}} = 54 \pm 4^\circ$ one obtains a maximum force of $\approx 8.7 \pm 1.4 \mu\text{N}$, which agrees with the measured values (fig. 2(a) and (b)).

A relevant question is how the pinning forces depend on the size of defects. Marsh *et al.* reported two regimes. For narrow defects, the force increases with defect width and, for larger defects, the force saturates [27]. Here, we measured the maximum value of the pinning force F_{DAFI} *vs.* defect radius R (fig. 4(b), blue data points). Then, we plotted the maximum value of the force determined by fitting the deformation of the contact line $\eta_{\text{drop}}(x_{\text{drop}}, t)$ (fig. 4(b), orange data points) and calculated the dominant force $F_{\text{top}}^{\text{d}}$ via eq. (6) (fig. 4(b), red data points). All forces overlap for defect radii ranging from 50 to 500 μm within the error of the experiment. The direct measurements by DAFI tend to result in slightly lower forces compared to the other two. We attribute the lower forces to a defect-induced elongation of the drop. The drop slightly stretches since the force is higher is when the rear contact line passes the defect. As a result, the drop's width w slightly decreases with CLD and according to eq. (1) the lateral adhesion force decreases.

Pinning forces are largely independent on drop size and sliding speed (see the SM, section “S10 volume or speed dependency of defect peak force”). Larger defects, with a $R > 500 \mu\text{m}$ were also measured but then satellite drops were left behind leading to a larger variation in pinning forces [28] (see the SM, section “S11 definition of satellite drop”). In an additional reference experiment, drops were slid over defects at different speeds. Our analysis reveals no dependence of the depinning force on speed in the range between 250 $\mu\text{m/s}$ and 10 cm/s .

Next, we calculate the spring constant of the defect-induced fringe by calculating the slope in the linear regime for different defect diameters and drop volumes (fig. 4(c), for error calculation see the SM, section “S12 Defect spring constant *vs.* defect size, from DAFI Measurements”). The plot shows that the fringe elasticity increases linearly with defect diameter. We expect this behavior because the fringe length increases linearly with defect diameter. Thus, according to eq. (6), the force increases linearly. Here, we neglect contributions from the glass capillary deflection of DAFI because they are one order of magnitude smaller than s in the linear regime (see the SM, section “S6 force extraction”).

Conclusion. – We measured and calculated the lateral force acting on drops while they slide over cylindrical model defects on hydrophobic surfaces. Even though the basic model of Joanny and de Gennes was derived for infinitesimal small defects, forces calculated by a slightly adapted model are in quantitative agreement with directly measured forces and the forces calculated by an analytical model.

The quantitative agreement even holds for defects reaching a size of 40% of the drop diameter. This agreement indicates that the capillary length for the cutoff length L in the theory is a good choice, which was recently debated [29]. In order to provide more insight into the assumptions of the model of Joanny and de Gennes, we

extrapolate the linear dependence to defect diameters of 0 (fig. 4(c)). This value should correspond to the fringe elasticity of an infinitesimal small defect as defined by Joanny and de Gennes [6] because for infinitesimally small defects, $s \cong \eta(x)$ at positions very close to the defect. Joanny's and de Gennes' proportionality factor was defined as $k = \pi\gamma/\ln(L/x)$. Using our extrapolated value of $\approx 17 \text{ mN/m}$, we calculate an x -value of $\approx 4 \mu\text{m}$, which is in agreement with a value of small linear dimension over which the force is acting [30].

Experimentally, for simple geometrical defects, such as the cylindrical ones used here, the pinning force can be directly calculated by the capillary equation. In general, the DAFI allows a direct measurement of forces caused by arbitrary shaped defects. Such measurements do not require contact line analysis, fitting or knowledge about defect's contact angles.

Our thanks go to GABRIELE SCHÄFER and AZADEH AGHILI SHARIFI for preparing model defects. We thank CHIRAG HINDUJA, KALOIAN KOYNOV, ALEXANDRE LAROCHE, ABINAV NAGA, and DORIS VOLLMER for fruitful discussions. We acknowledge financial support by the German Research Society (DFG) via the CRC 1194 (Project-ID 265191195) “Interaction between Transport and Wetting Processes”, project A06 and C07 and the Priority Programme 2171 Dynamic wetting of flexible, adaptive and switchable surfaces (BU 1556/36-1).

Data availability statement: The data that support the findings of this study are available upon reasonable request from the authors.

REFERENCES

- [1] DE GENNES P. G., *Rev. Mod. Phys.*, **57** (1985) 827.
- [2] COLLET P., CONINCK J. D., DUNLOP F. and REGNARD A., *Phys. Rev. Lett.*, **79** (1997) 3704.
- [3] GAO L. and MCCARTHY T. J., *Langmuir*, **22** (2006) 6234.
- [4] LHERMEROUT R., PERRIN H., ROLLEY E., ANDREOTTI B. and DAVITT K., *Nat. Commun.*, **7** (2016) 12545.
- [5] LHERMEROUT R. and DAVITT K., *Soft Matter*, **14** (2018) 8643.
- [6] JOANNY J. F. and DE GENNES P. G., *J. Chem. Phys.*, **81** (1984) 552.
- [7] NADKARNI G. D. and GAROFF S., *Europhys. Lett.*, **20** (1992) 523.
- [8] SNOELIER J. H. and ANDREOTTI B., *Annu. Rev. Fluid Mech.*, **45** (2013) 269.
- [9] PERRIN H., LHERMEROUT R., DAVITT K., ROLLEY E. and ANDREOTTI B., *Phys. Rev. Lett.*, **116** (2016) 184502.
- [10] SHANAHAN M. E. R., *J. Phys. D: Appl. Phys.*, **22** (1989) 1128.
- [11] MARSH J. A. and CAZABAT A. M., *Phys. Rev. Lett.*, **71** (1993) 2433.
- [12] DELMAS M., MONTHIOUX M. and ONDARUHU T., *Phys. Rev. Lett.*, **106** (2011) 136102.

-
- [13] LIIMATAINEN V., VUCKOVAC M., JOKINEN V., SARIOLA V., HOKKANEN M. J., ZHOU Q. and RAS R. H. A., *Nat. Commun.*, **8** (2017) 1798.
 - [14] PILAT D. W., PAPADOPOULOS P., SCHÄFFEL D., VOLLMER D., BERGER R. and BUTT H.-J., *Langmuir*, **28** (2012) 16812.
 - [15] QIAO S., LI S., LI Q., LI B., LIU K. and FENG X.-Q., *Langmuir*, **33** (2017) 13480.
 - [16] MANNETJE D. T., BANPURKAR A., KOPPELMAN H., DUTS M. H. G., VAN DEN ENDE D. and MUGELE F., *Langmuir*, **29** (2013) 9944.
 - [17] FRENKEL I. Y., *Sci. Press Moscow and Leningrad* (1948).
 - [18] BUZÁGH A. and WOLFRAM E., *Kolloid-Z.*, **157** (1958) 50.
 - [19] KAWASAKI K., *J. Colloid Sci.*, **15** (1960) 402.
 - [20] FURMIDGE C., *J. Colloid Sci.*, **17** (1962) 309.
 - [21] EXTRAND C. W. and KUMAGAI Y., *J. Colloid Interface Sci.*, **170** (1995) 515.
 - [22] ELSHERBINI A. and JACOBI A., *J. Colloid Interface Sci.*, **299** (2006) 841.
 - [23] SEMPREBON C. and BRINKMANN M., *Soft Matter*, **10** (2014) 3325.
 - [24] DE GENNES PIERRE-GILLES, BROCHARD-WYART FRANÇOISE, QUÉRÉ DAVID *et al.*, *Capillarity and Wetting Phenomena: Drops, Bubbles, Pearls, Waves*, Vol. **315** (Springer) 2004.
 - [25] CHECCO A., *EPL*, **85** (2009) 16002.
 - [26] GAO N., GEYER F., PILAT D. W., WOOH S., VOLLMER D., BUTT H.-J. and BERGER R., *Nat. Phys.*, **14** (2017) 191.
 - [27] MARSH J. A. and CAZABAT A. M., *Europhys. Lett.*, **23** (1993) 45.
 - [28] CHANG B., ZHOU Q., RAS R. H. A., SHAH A., WU Z. and HJORT K., *Appl. Phys. Lett.*, **108** (2016) 154102.
 - [29] TADMOR R., *Langmuir*, **37** (2021) 6357.
 - [30] RAPHAEL E. and JOANNY J. F., *Europhys. Lett.*, **21** (1993) 483.